CURRENT STATUS OF THE LUMIO AUTONOMOUS OPTICAL NAVIGATION EXPERIMENT

Paolo Panicucci[(1)], Felice Piccolo[(2)], Salvatore Borgia[(3)], Antonio Rizza[(4)], Vittorio Franzese[(5)], Francesco Topputo[(6)]

[(1)]Assistant Professor, Department of Aerospace Science and Technology, Politecnico di Milano, Via Giuseppe La Masa, 34, 20156 Milano, Italy, +39 02 2399 7157, paolo.panicucci@polimi.it
[(2)]PhD Student, Department of Aerospace Science and Technology, Politecnico di Milano, Via Giuseppe La Masa, 34, 20156 Milano, Italy, +39 02 2399 7157, felice.piccolo@polimi.it
[(3)]PhD Student, Department of Aerospace Science and Technology, Politecnico di Milano, Via Giuseppe La Masa, 34, 20156 Milano, Italy, +39 02 2399 7157, salvatore.borgia@polimi.it
[(4)]PhD Student, Department of Aerospace Science and Technology, Politecnico di Milano, Via Giuseppe La Masa, 34, 20156 Milano, Italy, +39 02 2399 7157, antonio.rizza@polimi.it
[(5)]Postdoc Fellow, Department of Aerospace Science and Technology, Politecnico di Milano, Via Giuseppe La Masa, 34, 20156 Milano, Italy, +39 02 2399 7157, vittorio.franzese@polimi.it
[(6)]Full Professor, Department of Aerospace Science and Technology, Politecnico di Milano, Via Giuseppe La Masa, 34, 20156 Milano, Italy, +39 02 2399 7157, francesco.topputo@polimi.it

ABSTRACT

While orbiting the Sun, the Earth-Moon system is periodically impacted by meteoroids. The scientific interest in these impacts relies on the possibility of gathering information about the formation and evolution of the Solar System. Moreover, in the context of future lunar robotic and human colonization, it is of primary importance to characterize the frequency and distribution of such impacts. Nowadays meteoroid observations are carried out from Earth-based observatories that cannot study the Moon farside impacts. In this context, the LUMIO mission wants to complement these observations to improve the current meteoroid models. LUMIO is a 12U CubeSat mission to Earth-Moon L_2 studying the meteoroid impacts on the lunar farside. Besides its scientific objectives, the LUMIO mission wants to demonstrate the feasibility of autonomous vision-based navigation at the Moon. This paper outlines the current status of the LUMIO optical navigation experiment by focusing on image processing and vision-based navigation filter design and implementation. Moreover, the image generation procedure is described. Finally, the vision-based navigation chain is tested on software-in-the-loop simulations for two different scenarios. Numerical results highlight the feasibility of navigating around the Moon from a distance between 35000 and 80000 km with velocity errors below 1 m/s and position errors below 200 km.

1 INTRODUCTION

The Earth-Moon system is constantly bombarded by meteoroids of different sizes. They are fragments of asteroids, comets, and major celestial bodies which provide information about the formation and evolution of the Solar System. Meteor showers have been studied for at least 50 years to construct Solar System meteoroid models which can be exploited to understand the spatial distribution of objects near the Earth-Moon system, to predict the degradation of spaceborne equipment, and to forecast

large impact on Earth [1]. These models have been constructed by performing Earth-based observations of meteor showers and lunar flashes due to meteoroid impacts. As Earth-based observations are limited by geometrical, illumination, and meteorological constraints, a Moon-orbiting observatory could increase the quality and quantities of meteoroid impact detection to improve current meteoroid models. To answer these questions, the Lunar Meteoroid Impacts Observer (LUMIO) mission has been designed and is currently in Phase B under ESA funding [2]. LUMIO is a CubeSat mission to a halo orbit at Earth-Moon L2 that shall observe, quantify, and characterize meteoroid impacts on the Lunar farside by detecting their flashes, complementing Earth-based observations on the Lunar nearside, to provide global information on the Lunar Meteoroid Environment and contribute to Lunar Situational Awareness [3, 4]. As part of the LUMIO mission objectives, the mission foresees proving the feasibility of autonomous vision-based navigation at the Moon. In this work, the optical navigation experiment performed by LUMIO is presented at its current development status focusing on the navigation performances and the vision-based navigation design.
The rest of the paper is structured as follows. Section 2 presents LUMIO by underlining the overall mission and the high-level spacecraft design at its current stage. Section 3 gives an overview of the Attitude & Orbit Control Subsystem (AOCS) of LUMIO. Then, Section 4 illustrates the process used within the LUMIO mission to simulate images to assess the optical navigation experiment performance. In Section 5 the image processing (IP) is presented in detail by outlining the IP performance. Section 6 presents the filter implementation by focusing on how to feed the navigation scheme with the IP measurement to guarantee bounded errors and correct state estimation. Finally, image-in-the-loop simulations are presented in Section 7 for two different scenarios to underline the filter performance with different illumination and Moon appearance in the image.

2 THE LUMIO MISSION

LUMIO is a CubeSat mission led by Politecnico di Milano to a halo orbit at Earth-Moon L_2. Politecnico di Milano's LUMIO mission envisages a 12U CubeSat integrated by Argotec equipped with a custom optical payload designed by Leonardo, a dedicated on-board payload data processing unit designed by S&T, a Solar Array Drive Assembly and X-band transponder developed by IMT, and the ground segment and operations in charge of Nautilus. The mission foresees the observation of the meteoroid impacts on the far side of the Moon so as to complement Earth-based observations which can only detect near side impact due to the tidally-locked motion of the Moon. The scientific payload, called LUMIO-Cam, is designed and built by Leonardo and it consists of a narrow-angle camera with two detectors providing the possibility of observing the flashes in the visible and the near-infrared spectra. This will improve the characterization of the meteoroid flux impacting the lunar surface advancing the understanding of how meteoroids evolve in cislunar space.
The LUMIO mission timeline, depicted in Figure 1, foresees a commissioning phase and a transfer phase lasting about 150 days where the spacecraft detumbles, performs the subsystems commissioning, and corrects the trajectory to target the Halo Injection Maneuer. This maneuver enables the spacecraft to insert into a halo orbit around the Earth-Moon L_2 point. The spacecraft will perform 1 year of nominal mission on the halo and it will end its life by impacting the Moon after having executed the End of Life Maneuver.
Thanks to the almost-periodic behavior of the halo orbits, the LUMIO concept of operation foresees two modes during its operative phase [5]: the Science Cycle and the Navigation & Engineering Cycle. The former lasts approximately 14 days and occurs when the Moon farside has the optimal illumination to perform flash detection (i.e., half of the Moon is not illuminated). The latter is defined as the complementary of the Science Cycle. During the Navigation & Engineering Cycle, the CubeSats cannot carry out scientific observations, therefore it can perform engineering activities, such as reaction

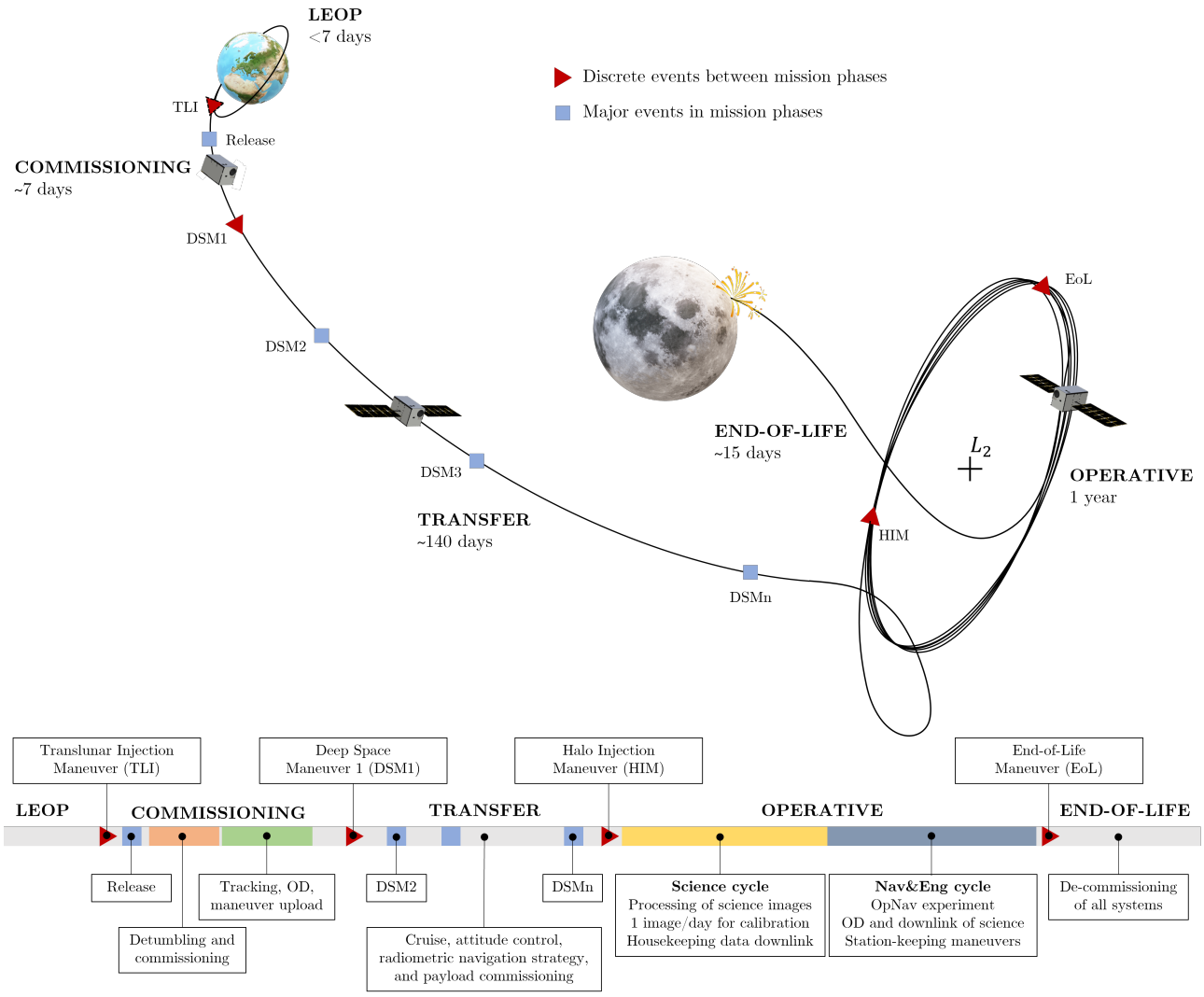

Figure 1: LUMIO mission timeline

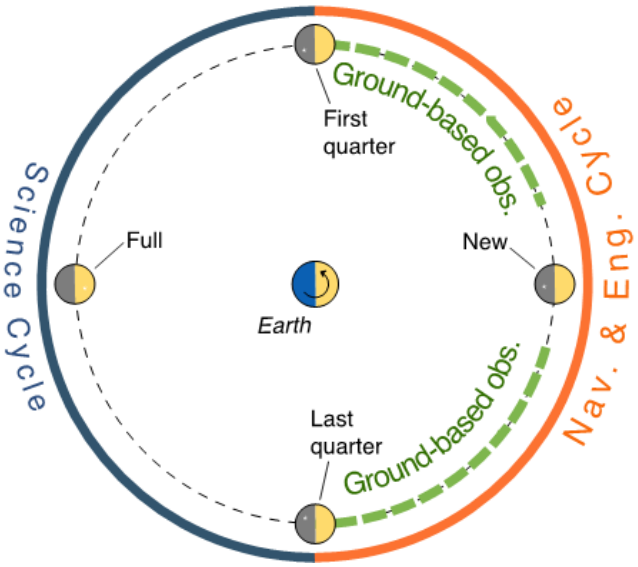

Figure 2: LUMIO concept of operation.

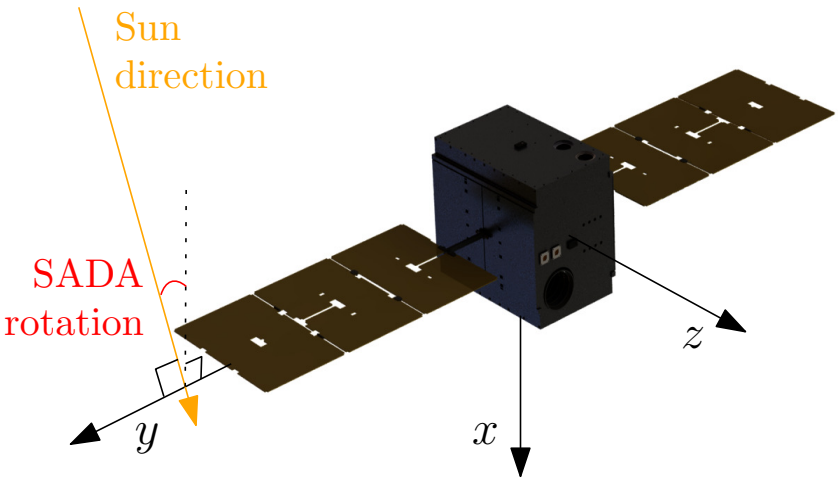

Figure 3: LUMIO pointing definition (Credits: Argotec)

wheel desaturation, communication with the Earth, station-keeping, and technological demonstration. A sketch of the LUMIO concept of operation is reported in Figure 2 for the sake of completeness. The LUMIO technological demonstration is the Optical Navigation Experiment (ONX) [6]. The ONX aims at proving the feasibility of CubeSats to autonomously navigate in the cislunar environment without communication with the ground by exploiting images of the Moon. Indeed, the spacecraft-Moon range is computed by determining the appearance of the Moon in the image [7–9]. This piece of information is then provided to the navigation filter to determine the spacecraft state [6]. Before describing the vision-based navigation (VBN) chain, the LUMIO AOCS architecture is presented to provide information about the system design ensuring the correct spacecraft pointing and orbit.

3 LUMIO AOCS ARCHITECTURE

The LUMIO platform, depicted in Figure 3 in its current configuration, must perform several operations during its lifetime which implies accurate pointing to the Moon to perform science and the ONX, to the Earth to communicate with the ground station, and to the Sun as secondary pointing to ensure power generation. Moreover, station-keeping and orbital correction maneuvers must be performed to ensure the operative orbit insertion, the 1-year nominal mission on the halo orbit, and the correct end-of-life impact on the Moon. The LUMIO pointing definition, shown in Figure 3, foresees the primary pointing towards the desired celestial body depending on the mission phase. Moreover, the secondary pointing must ensure that the Solar Array Drive Assembly axis, i.e., the axis around which the solar panels rotate, is perpendicular to the Sun direction. This reference pointing definition implies that the Sun moves on the x-z plane keeping its projection on the x-axis positive. Therefore, the Sun light as seen from the LUMIO-Cam arrives from a constant direction (i.e., the image x-axis). The AOCS subsystem is composed of:

1. The main propulsion system (PS) which is composed of a single thruster
2. A reaction control system (RCS) composed of 4 thrusters
3. A reaction wheels (RW) assembly composed of 4 wheels
4. Two star trackers in cold redundancy
5. A set of gyroscopes to support attitude determination when star trackers cannot operate

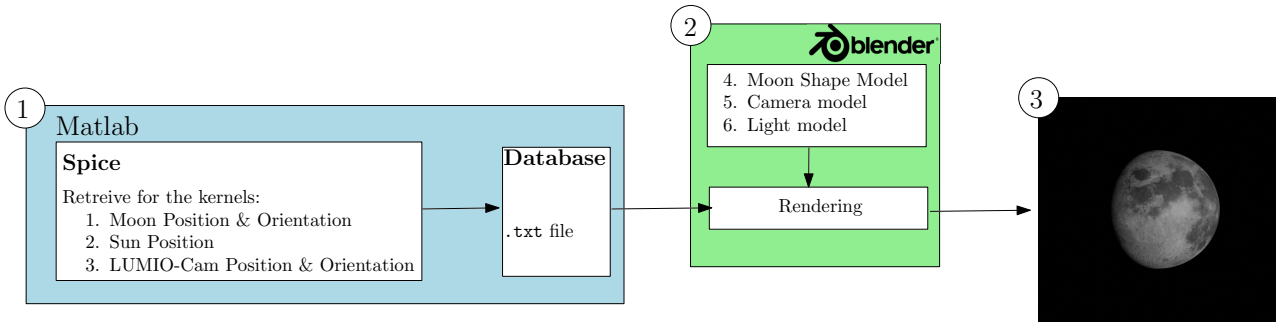

Figure 4: Image generation: 1) Geometry definition; 2) Observation properties; 3) Rendered image.

Table 1: LUMIO-Cam properties.

Resolution	Field Of View	Focal Length	Pixel Size	Optical Center
1024x1024 pixels	6.0 deg	127 mm	13.3 μm	(512, 512) pixels

6. Four sun sensors

The main PS performs orbital maneuvers during the whole mission. The RCS, together with the RWs, is responsible for the momentum management and attitude control of the platform. It is worth noting that the two star trackers are not meant to work simultaneously, but they are carried on the spacecraft in cold redundancy configuration to ensure robustness to the design in case of failure.

4 IMAGE GENERATION

To simulate the LUMIO optical navigation experiment, it is necessary to generate images of the Moon on the LUMIO operational orbit. To do so, a simulator has been implemented based on Blender. Blender can render images with path tracing by simulating the behaviors of light, materials, and sensors. The user must define the position and orientation of the objects in the scene (e.g., the camera, the Sun, and the Moon) and model the material to emulate the scattering law between the incident light on the object surfaces. Despite other rendering engines, such as ESA's PANGU [10] or Airbus Defence & Space's SurRender [11], are specifically designed for space applications with detailed modeling of light-material interaction and of space sensors. Nevertheless, Blender is preferred because it is an open-source software.
The image simulator developed is a combination of MATLAB and Blender, and its high-level architecture is shown in Figure 4. The generation of synthetic images of the Moon is performed through the following steps:

1. In MATLAB, the positions of LUMIO, the Moon, and the Sun are retrieved as a function of the epoch, along with their orientations. These data are provided by SPICE kernels and are exported into `.txt` files.

2. In Blender, the Moon is modeled by creating a 3D sphere with the Moon Digiteal Elevation Model and the Moon texture. The LUMIO-Cam properties are set by using the values in Table 1. The data from point 1) are used to define the LUMIO-Moon-Sun geometry.

3. The Blender engine reads parameters from 1) and 2) and renders the Moon image to be used for navigation by taking into account the Moon texture and digital elevation map.

This method is used to generate a dataset of images covering an entire Nav&Eng cycle.

5 IMAGE PROCESSING

The goal of the image processing is to determine the points belonging to the illuminated Moon limb in the image and use them to reconstruct the position vector of the Moon in the camera frame. Therefore a dedicated image processing pipeline has been designed and implemented. As outlined by Jonniaux et al. [12], the limb is a sharp feature that is convoluted with the camera Point Spread Function (PSF), leading to difficulties in reconstructing the exact limb location. Therefore, a sequential approach inspired by Christian [13] has been implemented for the LUMIO mission. The proposed approach allows the determination of the limb at subpixel precision and the rejection of possible outliers. The approach is divided into several steps.

First, by knowing the Sun direction from sun sensors or ephemerides, the projection of the Sun rays can be determined. The main idea is to scan the image in this direction to reconstruct the image intensity evolution along this scanning direction to detect the first rapid increase in pixel intensity. This could be associated with the Moon lit limb. As noted in Christian [13], it is important to determine only the directly illuminated limb even for low phase angles to avoid systematic errors in the vision-based navigation solution. Moreover, it is worth noting that the projection of the Sun direction could be deduced directly from the image as proposed in Mortari et al. [7], but numerical investigations have shown that the algorithm proposed in Mortari et al.'s work is not well-conditioned when the phase angle is close to zero, leading to unstable solution in determining the lit limb. The image is then scanned along the direction of the incoming light to determine the evolution of the pixel intensity. Lines are equally spaced in the image along the scanning direction to ensure the intersection between the lines and the Moon as shown in Figure 5.

Second, it is necessary to determine where the limb is along the scanned line. The limb is theoretically identified as a sharp change in intensity. Moreover, after the sharp change, the intensity stabilizes at a quite high value compared to the dark background. It is important not to select bright pixels due to cosmic rays, stars, or hot pixels when performing the coarse estimation of a limb point. Therefore, the scanned line is averaged by taking the mean of N_{mean} intensity values over the scanning line. This enables removing localized intensity variations in the scanning line which are not due to the limb. The coarse edge location is determined as the first pixel of a given interval of pixels whose intensity values are above a user-defined threshold τ_{thr}. The threshold τ_{thr} strongly depends on the SNR obtained during flight and calibration.

Third, a subpixel estimation of the limb location must be determined to obtain an accurate position estimation for the navigation filter. Indeed, the accuracy of the image processing position solution strongly relies on the accuracy in limb point determination, implying that a subpixel solution leads to a better measurement given to the filter. Therefore, a sequential refinement of the coarse solution is performed [13]. A patch of N_{patch} is extracted from the image around the selected coarse limb point and the Laplacian of Gaussian filter is used to determine a finer estimation of the limb location. The Laplacian of Gaussian is preferred over other edge-finding techniques as it searches for zero crossing of the second derivatives without any thresholding mechanism. The subpixel location of the limb is determined by using the Zernike-moment approach [13], which is preferred for its simplicity in implementation over more complex algorithms like the partial-area-effect method [14]. The proposed and implemented method is tested on synthetic images of the Moon determining the limb point location with subpixel accuracy. Figure 6 shows the error with respect to the true Moon limb for the aforementioned steps.

Finally, outlier rejection is performed by using the RANSAC (RANdom SAmple Consensus) algorithm [15] by fitting a circle on the subpixel limb points. The circle fitting is selected as the Moon flattening is 0.0012, leading to almost a perfect circle when projected in the image. Moreover, this simplifies the calculation and the error computation as the error between a point $\boldsymbol{P}$ to the circle limb

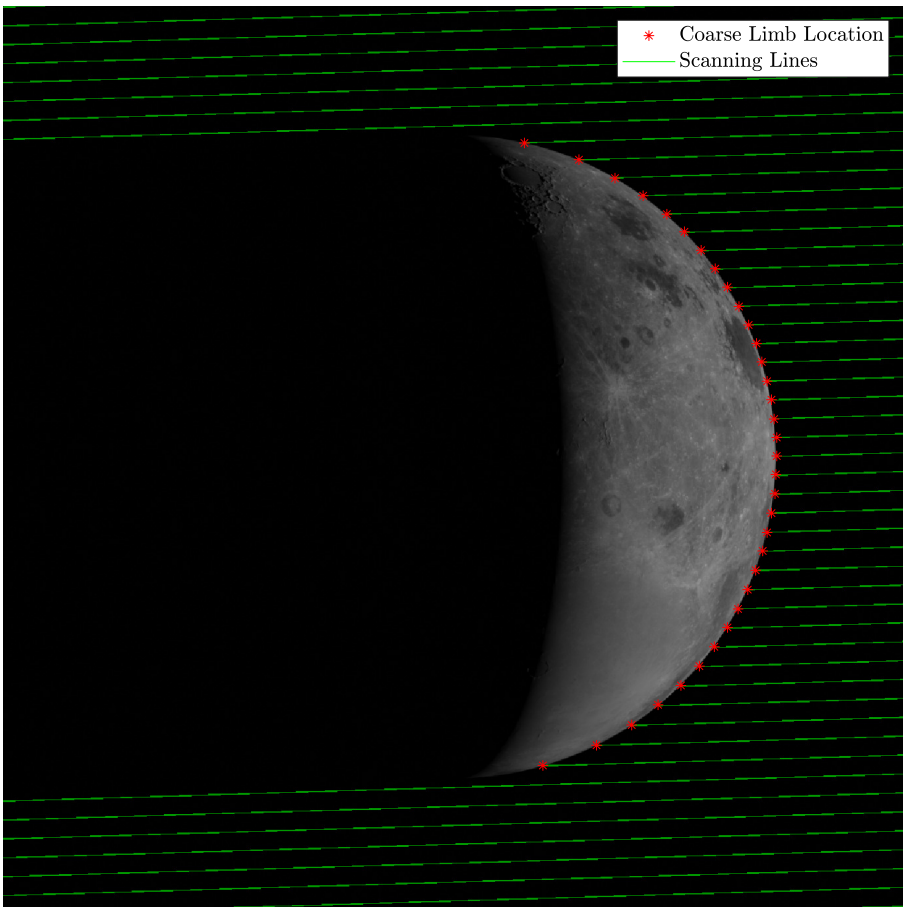

Figure 5: Example of the scanning procedure with 50 lines. Scaning lines are reported in green, while coarse limb points are reported with the red asterisks.

is computed as:

$$\epsilon = ||\boldsymbol{P} - \boldsymbol{C}|| - r \tag{1}$$

where $\boldsymbol{C}$ is the fit circle center and r is the fit circle radius. To avoid ill-conditioning of the RANSAC, candidate limb points are selected from different patches so to minimize the possibility of selecting nearby points. The performances of the algorithm after outlier rejection are reported in Figure 6. The limb points are determined with 0.2 pixels of standard deviation which is consistent with the setting provided to the RANSAC algorithm. The mean of the inliers is slightly biased, leading to a systematic error in the position solution provided to the filter (see also Section 6 for more details).
Once the inliers are identified, the limb points can be used to compute the optical observables. The optical observables depend on the implemented image processing algorithm (e.g., planet centroid and apparent diameter [16] or position vector [17]). For the LUMIO mission, it has been decided to estimate directly the position vector within the image processing pipeline to simplify the navigation filter implementation. The Moon projection is estimated by fitting a circle to the observed lit limb points, which are retrieved from 2D images as previously outlined. Let $[D]$ be the matrix containing on the diagonal the semimajor axes of the Moon ellipsoid, let $[PC]$ be the rotation matrix from the camera reference frame to the Moon principal axes reference frame, and let $[K]$ be the intrinsic camera matrix. The position estimation is estimated as follows Christian and Robinson [17]

$$\boldsymbol{r} = -\left([D]\,[PC]\right)^{-1}\left(\boldsymbol{n}^T\boldsymbol{n} - 1\right)^{-1/2}\boldsymbol{n} \tag{2}$$

where $\boldsymbol{r}$ is the camera-to-object position vector in the camera reference frame and $\boldsymbol{n}$ the solution to the least-squares problem in the Cholewsky decomposition space fitting the limb point location on the

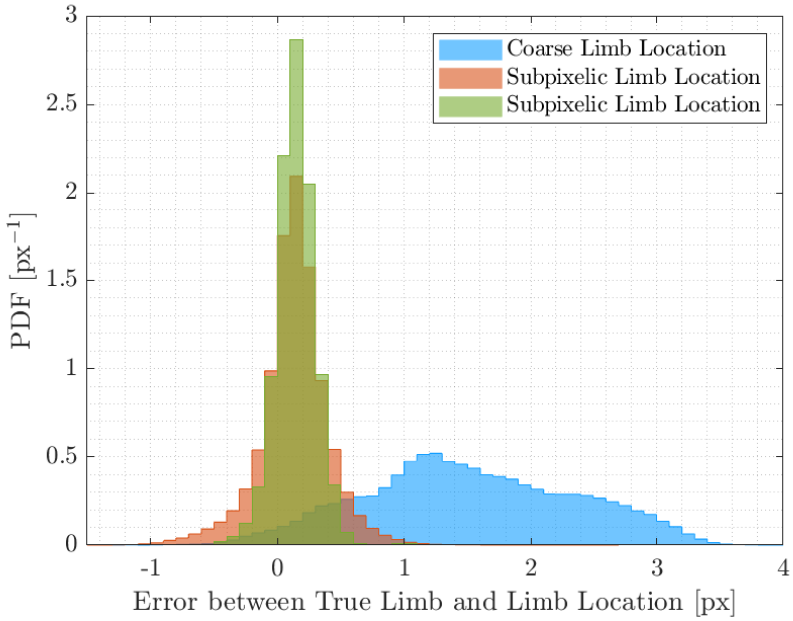

Figure 6: Error of the detected limb points at different stages of the IP chain.

Moon ellipsoid (see Christian and Robinson [17]).
The covariance is then computed by taking into account the error in the limb point location and in the attitude knowledge:

$$[P_{\boldsymbol{r}\,\boldsymbol{r}}] = [N]\,[P_{\boldsymbol{n}\,\boldsymbol{n}}]\,[N]^T + [Q]\,[P_{\boldsymbol{q}_v\,\boldsymbol{q}_v}]\,[Q]^T \tag{3}$$

where $[P_{\boldsymbol{n}\,\boldsymbol{n}}]$ is the covariance on vector $\boldsymbol{n}$ arising from the least square problem (see Christian and Robinson [17]), $[P_{\boldsymbol{q}_v\,\boldsymbol{q}_v}]$ is the covariance on the vectorial part of the inertial attitude knowledge, and $[F]$ and $[Q]$ are the derivatives of the position with respect to the limb point locations and the vectorial part of the inertial quaternion. In detail:

$$[N] = (\boldsymbol{n}^T\boldsymbol{n} - 1)^{-1/2}\,[PC]^T\,\left[D^{-1}\right]\left([\mathbb{1}_{3\times3}] - \frac{\boldsymbol{n}\boldsymbol{n}^T}{(\boldsymbol{n}^T\boldsymbol{n} - 1)}\right) \tag{4}$$

$$[Q] = 2(\boldsymbol{n}^T\boldsymbol{n} - 1)^{-1/2}\,[PC]^T\left[\left(D^{-1}\boldsymbol{n}\right)^{\wedge}\right] \tag{5}$$

where $[\mathbb{1}_{3\times3}]$ is the 3×3 identity matrix and $[\square^{\wedge}]$ is the skew-symmetric matrix associated with the cross product. To understand the performance of the image processing algorithm, the image processing is tested over a dataset of images generated with the procedure in Section 4 covering the first Nav&Eng cycle (i.e., about 15 days). The error of the proposed image processing pipeline is reported in Figure 7 along with the evolution of the phase angle and the Moon's apparent diameter. The image processing is not affected by illumination conditions as an illuminated limb is always visible in the image, as also noted by Jonniaux et al. [12]. Moreover, the performance of the image processing is not affected by errors in the Sun direction as outlined in numerical investigations - not reported here for the sake of brevity. The image processing performance is consistent with results from the literature affected by the Moon's apparent diameter. This is because a smaller Moon implies that fewer scanning lines are impacting the illuminated limb. The position error is below 200 km for most of the cases in the camera boresight direction, whereas it is below 10 km for the in-plane directions. Note that the error on the x-axis is higher as the Sun rays are coming from the positive axis direction. This leads to constraining the position estimation with higher accuracy on the y-axis and having a high correlation between the x-axis and the z-axis as shown in Figure 7.

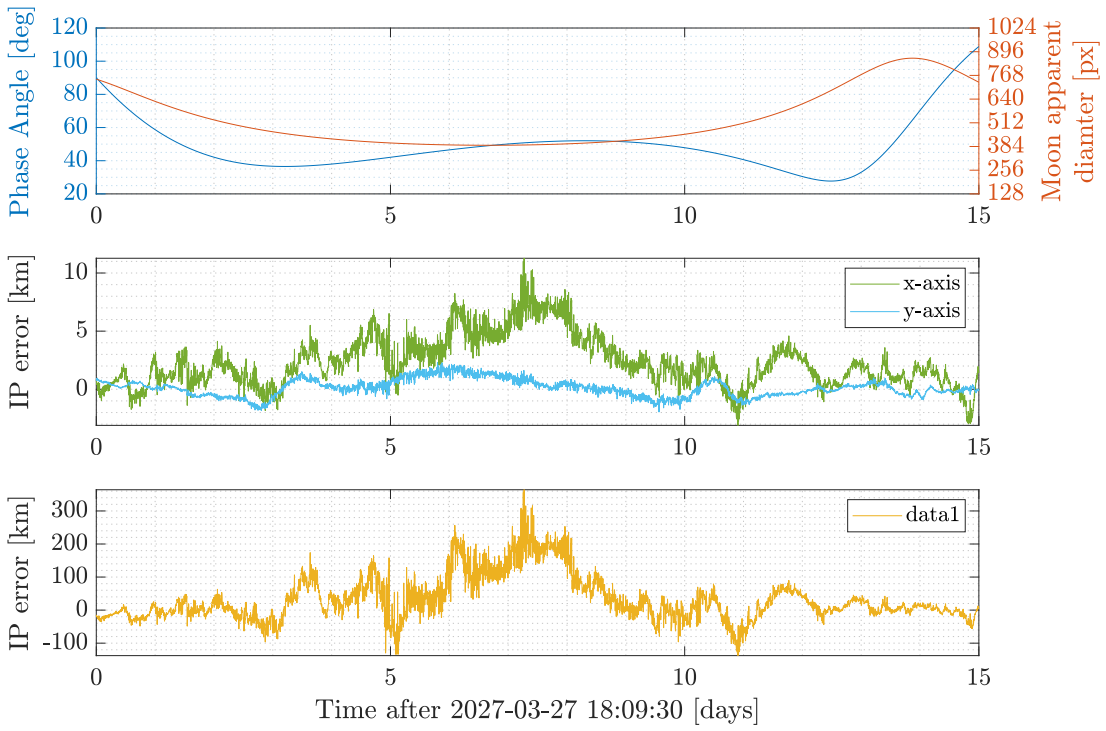

Figure 7: The image processing error on the Cartesian axes for the first Nav&Eng cycle. In the first plot, the evolution of the phase angle and the Moon apparent diameter is reported as well.

6 NAVIGATION FILTER

The navigation filter employed for the LUMIO optical navigation experiment is an Extended Kalman Filter (EKF). The estimated state vector is:

$$\boldsymbol{x} = \begin{bmatrix} \boldsymbol{r}^T & \boldsymbol{v}^T & \boldsymbol{a}_r^T & \boldsymbol{b}^T \end{bmatrix}^T \tag{6}$$

where $\boldsymbol{r}$ and $\boldsymbol{v}$ are the spacecraft position and velocity, expressed in the J2000 reference frame centered in the Earth-Moon barycenter, $\boldsymbol{a}_r$ is a 3x1 vector of residual accelerations and $\boldsymbol{b}$ is a 3x1 vector of image processing biases. The latter two are modelled as first order Gauss-Markov processes [18]. The spacecraft position and velocity are propagated by integrating a dynamical model that accounts for the gravitational attraction of the Moon, the Earth, the Sun and the estimated residual accelerations. The propagation is based on a Runge-Kutta 4 integration scheme. The state transition matrix (STM) is also integrated together with the equations of motion.
The EKF measurement model is given by:

$$\boldsymbol{h}(\boldsymbol{x}) = -\left[CN\right](\boldsymbol{r} - \boldsymbol{r_M}) + \boldsymbol{b} \tag{7}$$

$$[H] = \left[\frac{\partial \boldsymbol{h}}{\partial \boldsymbol{x}}\right] = \begin{bmatrix} -\left[CN\right] & [\mathbb{0}_{3\times3}] & [\mathbb{0}_{3\times3}] & [\mathbb{1}_{3\times3}] \end{bmatrix} \tag{8}$$

where $\boldsymbol{r_M}$ is the position vector of the Moon, $[CN]$ is the rotation matrix from the J2000 frame to the LUMIO camera frame, and $[\mathbb{0}_{3\times3}]$ is the 3×3 zero matrix. $[CN]$ is computed as:

$$[CN] = [CB]\,[BN] \tag{9}$$

in which $[BN]$ is the rotation matrix from the J2000 frame to the LUMIO body frame and $[CB]$ is the rotation matrix from the LUMIO body frame to the LUMIO camera frame. The former is provided

by the AOCS subsystem, and the latter is assumed to be known. The measurement covariance matrix used in the EKF update is provided by the IP algorithm (see Eq. 3). It accounts both for the uncertainty in the estimation of the spacecraft position from the extracted limb points and for the attitude uncertainty.

7 NUMERICAL RESULTS

The proposed numerical simulations investigate the performance of the VBN chain in two different scenarios. In both scenarios, the images are rendered with the reference attitude on the reference trajectory to obtain a reference dataset to be used in all the simulations (see Section 4). Then the initial spacecraft position and orientation are perturbed to take into account initial state errors. Moreover, the attitude of the spacecraft is perturbed according to the attitude knowledge requirement. Moreover, an error of 5 degrees is added to the Sun direction estimation from star trackers to take into account image processing errors arising from light direction errors. In the proposed implementation images are processed sequentially every 300 seconds and the image processing algorithm provides the position estimate and its covariance to the navigation algorithm that determines the spacecraft states. To have a preliminary assessment of the statistical performance of the navigation filter, a Monte Carlo simulation with 100 samples is performed by perturbing the sensor measurements and the initial spacecraft state.
In the first scenario, the first three days of the Nav&Eng cycle are simulated to study the VBN chain results when the moon occupies the majority of the field of view as shown in Figure 8a. This implies that more points are detected when scanning the image searching for the Moon limbs, leading to a more accurate estimation of the spacecraft position with respect to the Moon. Moreover, the spacecraft orbits closer to the moon when the dynamics is less linear, leading to a worse performance of the navigation filter. In the second scenario, the furthest positions in the first Nav&Eng cycle (e.i, from 6 to 9 days) are simulated to understand the performance of the algorithm when the Moon is smaller in the image as shown in Figure 8b. This leads to detecting fewer points, implying less accurate and precise image processing measurements.

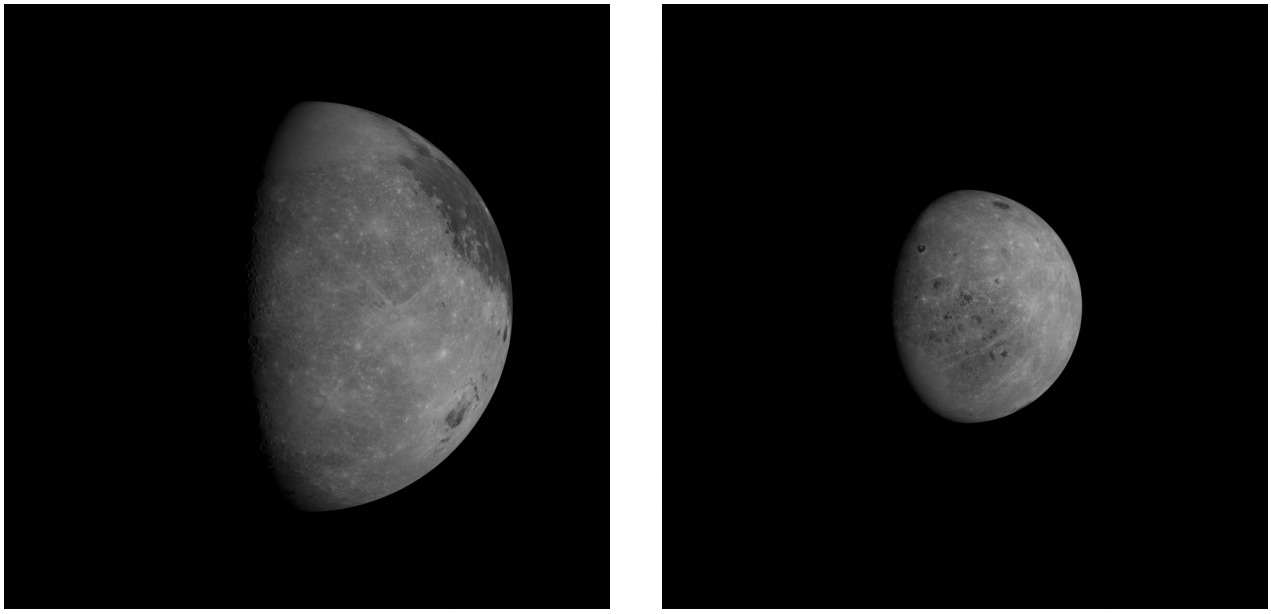

(a) Scenario 1 (b) Scenario 2

Figure 8: Example of images in the two considered navigation scenarios.

7.1 Scenario 1: Closest range to the Moon

The results in terms of position and velocity in the camera frame for the Monte Carlo simulation of the first scenario are reported in Figures 9 and 10. The filter converges rapidly despite the spacecraft is orbiting in the more non-linear part of the orbit. This is due to the accuracy and precision of the image processing measurement (see Figure 7) which show low variability with respect to the true position. As mentioned before, this is because a high percentage of lines scanning the image impact the Moon limbs, leading to a higher number of points to determine the position. Moreover, as the most informative points to constrain the conic fitting are the ones with the highest curvature, the probability to detect these points is higher, leading to a more precise solution from the image processing. The position is estimated with an error below 100 km for the z-axis and 10 km for the x-axis and y-axis. Moreover, the covariance bounds are below 200 km for the z-axis and 20 km for the x-axis and y-axis. This is consistent with vision-based navigation techniques that can provide accurate measurement in the image plane, while less precise orbit determination on the camera boresight. The velocity is well determined as well with an error below 1 m/s for the z-axis and 0.5 m/s m for the x-axis and y-axis. the velocity covariance bound converges to about 4 m/s for the z-axis and 1.5 m/s m for the x-axis and y-axis. The covariance bounds are overall larger than the spacecraft state error, but this is mainly because the filter has been tuned to work on the integrity of the orbit, leading to a larger covariance bound with respect to the filter estimation.

7.2 Scenario 2: Furthest range to the Moon

The results for the second scenario are presented in Figures 11 and 12 showing the position and the velocity of the spacecraft with respect to the Moon in the camera frame. The filter results show worse performance than the previous case mainly for the lower accuracy and precision of the image processing measurements (see Figure 7). Indeed, the number of scanning lines is fixed to 150 due to computational constraints, implying that few scanning lines detect Moon limbs and only a few of those are the informative ones with high curvature. This implies that the image processing solution is more noisy and less accurate in the simulated time frame. The introduction of the measurement bias as a Gauss-Markov process tries to mitigate this effect by estimating the IP systematic error from the measurement time series, but the observability of this systematic error is limited by the errors in the dynamics modeling in the filter and the IP random errors. Nevertheless, the effect of the systematic error is counteracted by the bias estimation performed in the filter, leading to a lower systematic error in the filtered results.
The position is estimated with an error below 200 km for the z-axis and 10 km for the x-axis and y-axis. Moreover, the covariance bounds are below 200 km for the z-axis and 20 km for the x-axis and y-axis. It is possible to notice that a systematic error is still present in the position estimate despite the slight correction obtained by the modeled bias. The systematic error is mainly present on the z- and x-axis because they are strongly correlated due to the constant light direction (see Figure 7 for correlation in the IP measurement and Section 3 for more details). It is important to note that the bias in the position is mainly due to the subpixel determination algorithm which is strongly dependent on the camera's optical response. In future phases of the mission, a better characterization of the optical payload could lead to design a dedicated subpixel filter to limit this effect. The systematic error is also visible on the z-axis velocity even though the estimation converges to 1 m/s on each axis. The velocity covariance bounds stabilize to 2 m/s for the z- and x-axis due to the measurement correlation and 0.5 m/s m for the y-axis. It is worth noting the slight systematic error in the velocity estimation due to the inaccuracy of the image processing measurement.

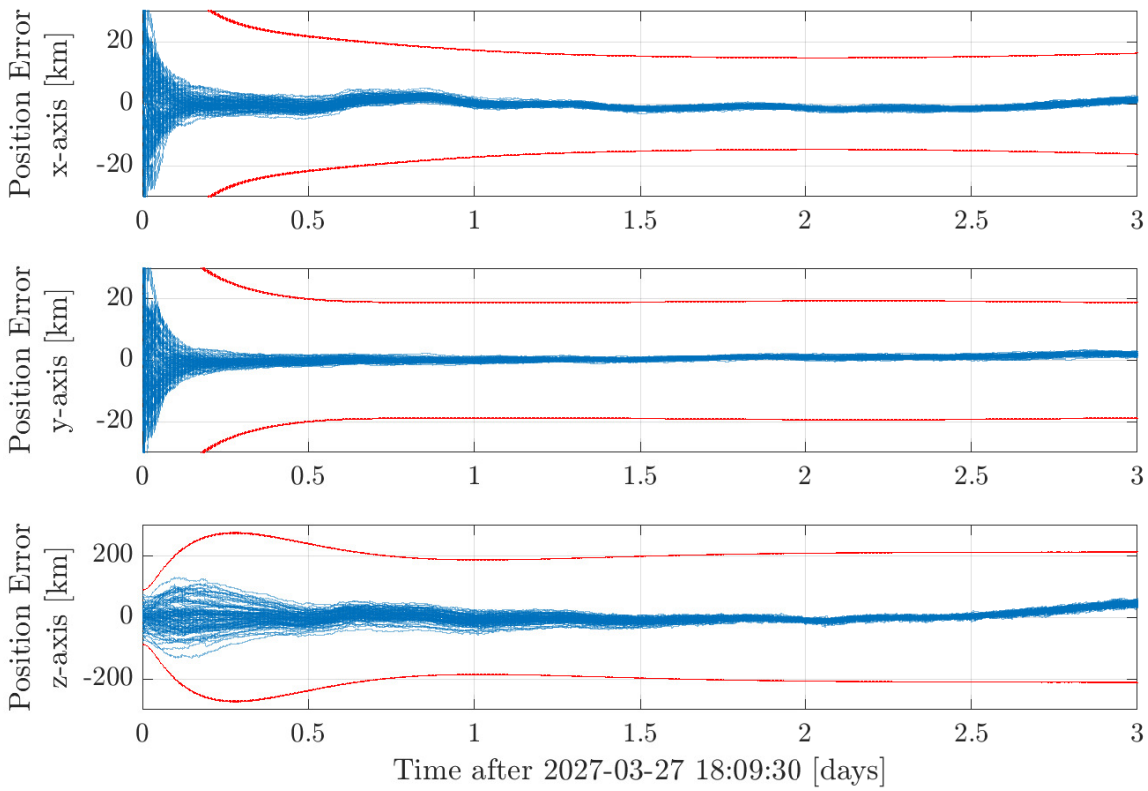

Figure 9: The Monte Carlo results in terms of position error in the camera frame for the first three days after the beginning of the first Nav&Eng Cycle.

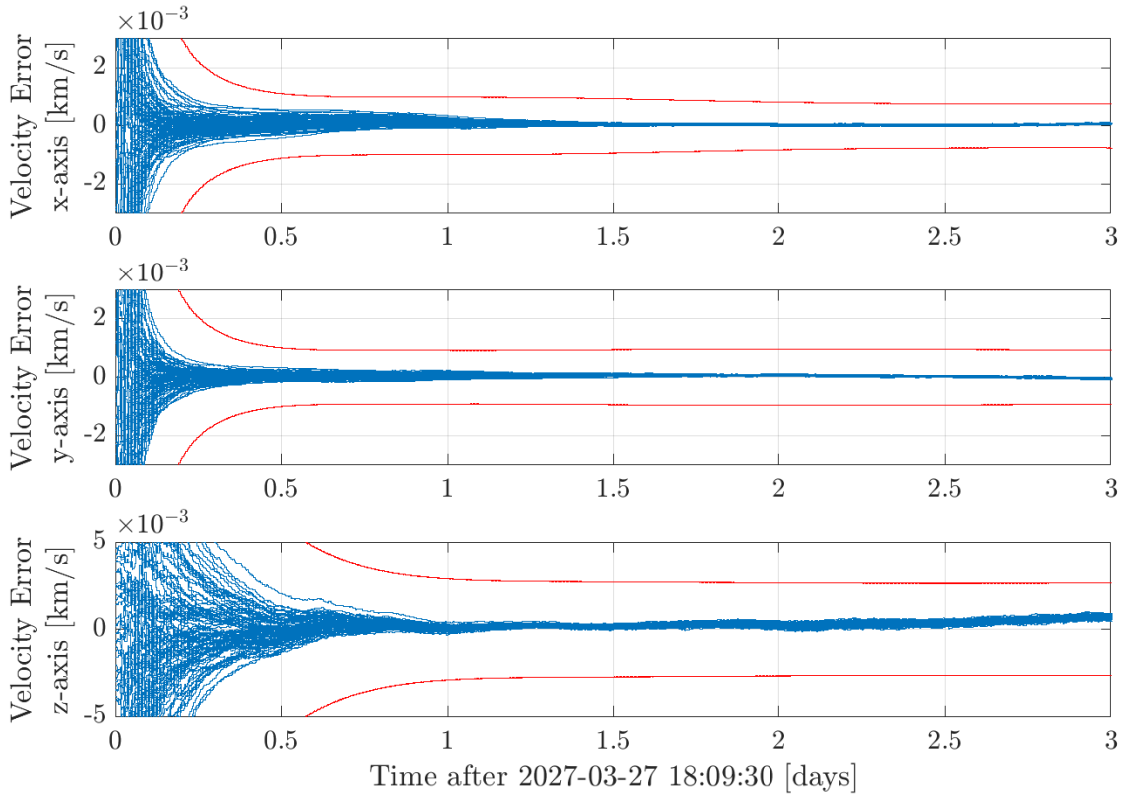

Figure 10: The Monte Carlo results in terms of velocity error in the camera frame for the first three days after the beginning of the first Nav&Egn Cycle.

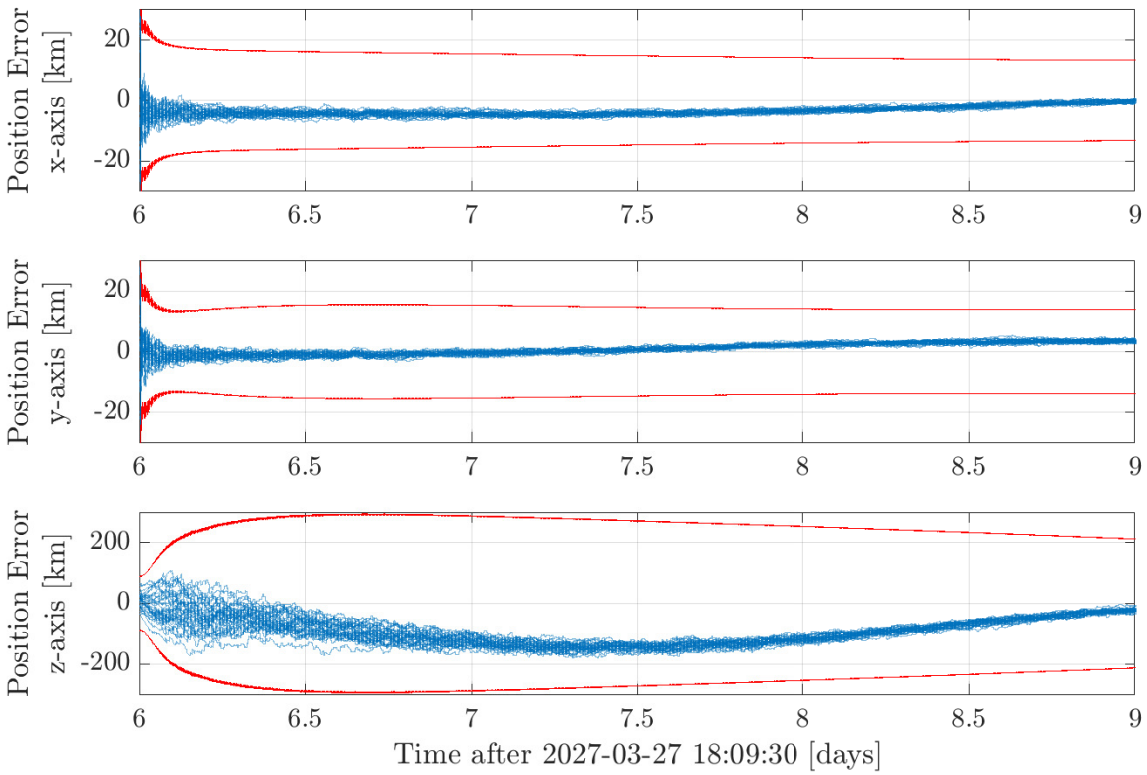

Figure 11: The Monte Carlo results in terms of position error in the camera frame from the 6th day to the 9th day after the beginning of the first Nav&Eng Cycle.

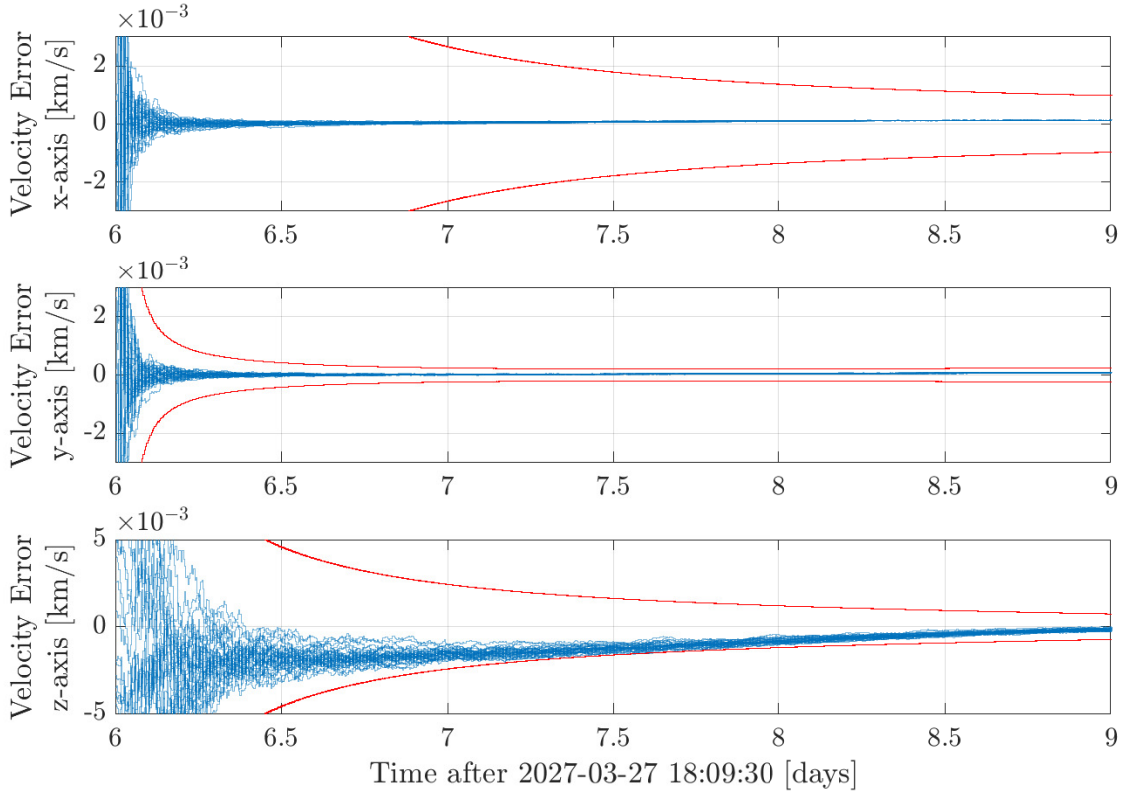

Figure 12: The Monte Carlo results in terms of velocity error in the camera frame from the 6th day to the 9th day after the beginning of the first Nav&Eng Cycle.

8 CONCLUSIONS

This paper outlines the current status of the optical navigation experiment that will be performed by LUMIO as a technological demonstration. After giving an overview of the LUMIO mission and the overall architecture of the AOCS subsystem, the paper focuses on the image processing algorithm and the navigation filter design. LUMIO exploits images of the Moon to navigate around the celestial body. The image processing can detect at subpixel precision and accuracy the Moon limbs and determine an estimate of the spacecraft-Moon position in the camera frame. IP results show that the position estimation can be performed with an error below hundreds of kilometers depending on the image processing setting. The image processing measurements are processed in a navigation filter to gather the full spacecraft state and to clean the image processing position estimation from errors. The designed filter includes in the estimated state the measurement bias and non-modeled accelerations to increase the robustness to systematic error and unmodeled dynamics. The filter is tuned to work in the whole Nav&Eng cycle and numerical investigation is performed on two selected scenarios of 3 days to assess the navigation performance. Performance is satisfactory providing estimation of less than 20 km on the camera plane axes and less than 200 km on the camera boresight. The velocity is well estimated as well with errors less than 1.5 m/s on the camera plane axes and less than 4 m/s on the camera boresight.
Future work should investigate the implementation of less computational-expensive image processing to increase the filter frequency. This would allow to have more measurements to better estimate the systematic error and shrink the covariance. Moreover, hardware-in-the-loop simulations should be performed to assess the robustness of the designed algorithm to real camera errors and to assess the computational effort on real processors.

ACKNOWLEDGMENT

This work has been conducted under ESA Contract No. 4000139301/22/NL/AS within the General Support Technology Programme (GSTP) through the support of the national delegations of Italy (ASI) and Norway (NOSA). The authors would like to acknowledge the members of the LUMIO team for their support and the ESA experts for reviewing the Phases 0 and A design.

REFERENCES

[1] Z. Ceplecha, J. Borovička, W. G. Elford, D. O. ReVelle, R. L. Hawkes, V. Porubčan, and M. Šimek. Meteor phenomena and bodies. *Space Science Reviews*, 84(3):327–471, 1998. doi: 10.1023/A:1005069928850.

[2] A. Cervone, F. Topputo, S. Speretta, A. Menicucci, E. Turan, P. Di Lizia, M. Massari, V. Franzese, C. Giordano, G. Merisio, D. Labate, G. Pilato, E. Costa, E. Bertels, A. Thorvaldsen, A. Kukharenka, J. Vennekens, and R. Walker. LUMIO: A CubeSat for observing and characterizing micro-meteoroid impacts on the Lunar far side. *Acta Astronautica*, 195:309–317, 2022. doi: 10.1016/j.actaastro.2022.03.032.

[3] F. Topputo, G. Merisio, V. Franzese, C. Giordano, M. Massari, G. Pilato, D. Labate, A. Cervone, S. Speretta, A. Menicucci, E. Turan, E. Bertels, J. Vennekens, R. Walker, and D. Koschny. Meteoroids detection with the LUMIO lunar CubeSat. *Icarus*, 389:115213, 2023. doi: 10.1016/j.icarus.2022.115213.

[4] G. Merisio and F. Topputo. Present-day model of lunar meteoroids and their impact flashes for LUMIO mission. *Icarus*, 389:115180, 2023. doi: 10.1016/j.icarus.2022.115180.

[5] A. M. Cipriano, D. A. Dei Tos, and F. Topputo. Orbit design for LUMIO: The lunar meteoroid impacts observer. *Frontiers in Astronomy and Space Sciences*, 5:29, 2018. doi: 10.3389/fspas.2018.00029.

[6] V. Franzese, P. Di Lizia, and F. Topputo. Autonomous optical navigation for the lunar meteoroid impacts observer. *Journal of Guidance, Control, and Dynamics*, 42(7):1579–1586, 2019. doi: 10.2514/1.G003999.

[7] D. Mortari, C. N. D'Souza, and R. Zanetti. Image processing of illuminated ellipsoid. *Journal of Spacecraft and Rockets*, 53(3):448–456, 2016. doi: 10.2514/1.A33342.

[8] J. A. Christian. Optical navigation using planet's centroid and apparent diameter in image. *Journal of guidance, control, and dynamics*, 38(2):192–204, 2015. doi: 10.2514/1.G000872.

[9] John A Christian. A tutorial on horizon-based optical navigation and attitude determination with space imaging systems. *IEEE Access*, 9:19819–19853, 2021.

[10] N. Rowell, S. Parkes, M. Dunstan, and O. Dubois-Matra. PANGU: Virtual spacecraft image generation. In *5th Int. Conf. on Astrodynamics Tools and Techniques, ICATT*, 2012.

[11] J. Lebreton, R. Brochard, M. Baudry, G. Jonniaux, A. H. Salah, K. Kanani, M. Le Goff, A. Masson, N. Ollagnier, P. Panicucci, A. Proag, and C. Robin. Image Simulation for Space Applications with the SurRender Software. In *Proceedings of the 11th International ESA Conference on Guidance, Navigation & Control Systems, 22 - 25 June 2021, Virtual*, 2021.

[12] Gregory Jonniaux, Keyvan Kanani, Pascala Regnier, and Daniele Gherardi. Autonomous vision-based navigation for JUICE. In *67th International Astronautical Congress, IAC-16 A*, volume 3, page 5, 2016.

[13] J. A. Christian. Accurate planetary limb localization for image-based spacecraft navigation. *Journal of Spacecraft and Rockets*, 54(3):708–730, 2017. doi: 10.2514/1.A33692.

[14] Agustín Trujillo-Pino, Karl Krissian, Miguel Alemán-Flores, and Daniel Santana-Cedrés. Accurate subpixel edge location based on partial area effect. *Image and Vision Computing*, 31(1):72–90, 2013.

[15] R. Hartley and A. Zisserman. *Multiple view geometry in computer vision*. Cambridge university press, 2003.

[16] John A Christian. Optical navigation using iterative horizon reprojection. *Journal of Guidance, Control, and Dynamics*, 39(5):1092–1103.

[17] John A Christian and Shane B Robinson. Noniterative Horizon-Based optical navigation by cholesky factorization. *Journal of Guidance, Control, and Dynamics*, 39(12):2757–2765, 2016. doi: 10.2514/1.G000539.

[18] Bob Schutz, Byron Tapley, and George H Born. *Statistical orbit determination*. Elsevier, 2004.